Grazing incidence small-angle x-ray scattering study of buried and free-standing SiGe islands in a SiGe/Si superlattice

J. Stangl, V. Holý,* T. Roch, A. Daniel, and G. Bauer
Institut für Halbleiterphysik, Johannes Kepler Universität, A-4040 Linz, Austria

J. Zhu, K. Brunner, and G. Abstreiter
Walter Schottky Institut (WSI), TU München, D-85748 Garching, Germany
(Received 10 May 2000)

We present a method to interpret reciprocal-space maps recorded in grazing-incidence small-angle x-ray scattering geometry to obtain the shape and the lateral correlation properties of *buried* islands. From the maps, which have been recorded for various penetration depths, the autocorrelation function is calculated, from which the island parameters are obtained by comparison with simulations based on the distorted-wave Born approximation. As a demonstration of the sensitivity of the method, measurements on self-organized SiGe islands in a Si/SiGe multilayer have been performed. It was possible to detect different shapes of the islands at the sample surface and those embedded in the multilayer. For a comparison with atomic force microscopy, we employ the same method to analyze images of the islands at the top surface.

I. INTRODUCTION

The shape of quantum dots has considerable influence on their electronic properties, and hence a variety of studies on self-organized quantum dots addresses the determination of their shape and its dependence on the growth conditions.[1,2] For free-standing dots, atomic force microscopy (AFM) is widely used to obtain this information. However, for virtually any structure in a practical application, the dots have to be overgrown. It is known that this often is accompanied by a considerable change of the size and shape of quantum dots, e.g., due to interdiffusion and segregation.[3,4] Hence methods are required that allow for the characterization of *buried* quantum dots. In addition to transmission electron microscopy (TEM), which yields ''direct images'' of the dots, but is limited to small sample areas and requires elaborate sample preparation, x-ray scattering techniques have successfully been applied to the study of dots embedded in a matrix[5–7] as well as dots fabricated by photolithography and etching.[8]

Several studies utilizing different scattering techniques exist, e.g., Kegel *et al.* have performed grazing-incidence diffraction (GID) investigations on the relaxation and interdiffusion of free-standing InAs dots on GaAs (001).[9] Wiebach *et al.* employed coplanar x-ray diffraction to study the interdiffusion of SiGe islands on Si(001).[10] In these studies, x-ray diffraction experiments that are sensitive to shape *and* strain have been performed. In order to identify solely the *shape* of buried dots, the scattered intensity around the origin of reciprocal space, i.e., the (000) Bragg reflection, can be used. Schmidbauer *et al.*[11] have investigated semiquantitatively the shape and lateral correlation of large free-standing Ge islands on a Si(001) surface using grazing-incidence small-angle x-ray scattering[12,13] (GISAXS) and AFM. Rauscher *et al.* investigated pyramidally shaped Ge islands on Si(111) using GID and GISAXS.[14] GISAXS has also been used in a semiquantitative study of buried $Si_{1-x-y}Ge_xC_y$ dots in a $Si_{1-x-y}Ge_xC_y$ multilayer.[15]

In this paper, we present an approach for the quantitative interpretation of GISAXS data. Describing the scattering process in the framework of the distorted-wave Born approximation,[16] it is possible to obtain information on the shape and the positional correlation of buried, as well as free-standing, quantum dots. For this purpose, two-dimensional reciprocal-space maps (RSM's) are recorded in GISAXS geometry for various penetration depths, i.e., for various vertical momentum transfer values. From these maps, the autocorrelation spectra can be calculated, which are simulated using a short-range-order model of the dot positions and different models of the shape of the quantum dots.

As a test for our method, we have performed GISAXS measurements on SiGe islands embedded in a Si/SiGe superlattice on (001)-oriented Si. On the top surface of the sample a dot layer with different parameters than those within the superlattice was grown. From the measurements, we can clearly distinguish between the islands at the sample surface, and those within the superlattice, demonstrating the sensitivity of our method. For the top layer, AFM investigations have been carried out, and the shape and correlation properties of the dots are analyzed by the same method as the x-ray data to allow for a direct comparison. It turned out that the sample is quite inhomogeneous laterally, so that the data obtained from AFM at different spots on the sample are not equivalent, but the shape resolution is very good. With GISAXS, on the other hand, we obtain good average parameters for dot shape and correlation, as here we integrate over much larger sample areas, and we can additionally obtain information on the *buried* dot layers.

The paper is organized as follows: In Sec. II the theoretical model is presented in detail. Section III presents the experimental results; in Sec. III B the GISAXS measurements are discussed, and Sec. III C presents the AFM results and gives a comparison of the x-ray data. Finally, Sec. IV presents the conclusions.

 ©2000 The American Physical Society

II. THEORY

Our description of x-ray scattering is based on distorted-wave Born approximation[16] (DWBA). Within this approach, the scattering potential $\hat{\mathbf{V}}$ of the sample is divided into two parts $\hat{\mathbf{V}}=\hat{\mathbf{V}}_A+\hat{\mathbf{V}}_B$, where $\hat{\mathbf{V}}_A$ describes the undisturbed system (a semi-infinite Si substrate in our case) and $\hat{\mathbf{V}}_B$ accounts for the multilayer structure and for the dots. The differential cross section of the scattering process is given by[16]

$$\frac{d\sigma}{d\omega}=\frac{1}{16\pi^2}\langle|\langle E_f^{(A)}|\hat{\mathbf{V}}_A|E_i^{(0)}\rangle+\langle E_f^{(A)}|\hat{\mathbf{V}}_B|E_i^{(A)}\rangle|^2\rangle, \quad (1)$$

where the averaging $\langle\rangle$ in Eq. (1) is performed over all random configurations of the dots in the multilayer. $|E_i^{(A)}\rangle$ and $|E_f^{(A)}\rangle$ are two independent eigensolutions of the wave equation with the scattering potential $\hat{\mathbf{V}}_A$; the latter one is time-inverted. $|E_i^{(0)}\rangle$ is the incident vacuum wave corresponding to $|E_i^{(A)}\rangle$, the vacuum wave $|E_f^{(0)}\rangle$ corresponding to $|E_f^{(A)}\rangle$ is the actual scattered wave. The vacuum waves $|E_{i,f}^{(0)}\rangle$ are assumed to be plane waves with wave vectors $\mathbf{K}_i$ and $\mathbf{K}_f$, respectively.

In the semi-infinite substrate, the eigensolutions $|E_{i,f}^{(A)}\rangle$ are represented by the plane waves

$$|E_i^{(A)}\rangle=t_i e^{i\mathbf{k}_i\cdot\mathbf{r}}, \quad |E_f^{(A)}\rangle=t_f^* e^{i\mathbf{k}_f^*\cdot\mathbf{r}}, \quad (2)$$

where $t_{i,f}$ are the Fresnel transmittivities of the surface corresponding to $|E_{i,f}^{(A)}\rangle$, and $\mathbf{k}_{i,f}$ are the wave vectors of the transmitted waves (corrected to refraction at the surface and to absorption in the substrate).

The disturbance $\hat{\mathbf{V}}_B$ of the scattering potential consists of two parts $\hat{\mathbf{V}}_B=\hat{\mathbf{V}}_{B,\mathrm{SL}}+\hat{\mathbf{V}}_{B,\mathrm{dots}}$ corresponding to the planar superlattice structure and to the dots, respectively. In the following, we restrict ourselves to nonspecular (diffuse) x-ray scattering. Due to the lateral homogeneity of the sample, the terms $\hat{\mathbf{V}}_A$, $\hat{\mathbf{V}}_{B,\mathrm{SL}}$, and $\langle\hat{\mathbf{V}}_{B,\mathrm{dots}}\rangle$ are translationally invariant and contribute consequently only to the specular scattering. Thus, the diffuse component of the differential scattering cross section is given by

$$\left(\frac{d\sigma}{d\omega}\right)_{\mathrm{diff}}=\frac{1}{16\pi^2}\langle|\langle E_f^{(A)}|\hat{\mathbf{V}}_{B,\mathrm{dots}}|E_i^{(A)}\rangle|^2\rangle. \quad (3)$$

With the small-angle scattering potential

$$\hat{\mathbf{V}}(\mathbf{r})=2K^2\delta(\mathbf{r}),$$

where $K=2\pi/\lambda$ is the wave-vector length in vacuum, $\delta(\mathbf{r})=1-n(\mathbf{r})$, and $n(\mathbf{r})$ is the local x-ray refraction index in the sample, the dot component $\hat{\mathbf{V}}_{B,\mathrm{dots}}$ of the scattering potential can be expressed as

$$\hat{\mathbf{V}}_{B,\mathrm{dots}}=2K^2\Delta\delta\sum_m \Omega(\mathbf{r}-\mathbf{R}_m), \quad (4)$$

using the mean shape function of a single dot $\Omega(\mathbf{r})$ (unity inside the dot, zero outside) and the random position $\mathbf{R}_m$ of the mth dot. From Eqs. (3), (4), and (2) we obtain for the diffuse scattering cross section

$$\left(\frac{d\sigma}{d\omega}\right)_{\mathrm{diff}}=\frac{K^2}{4\pi^2}|\Delta\delta|^2|t_i t_f|^2|\Omega^{\mathrm{FT}}(\mathbf{q})|^2 G(\mathbf{q}), \quad (5)$$

where $\Delta\delta$ is the contrast of the refractive indices of the dot and its neighborhood, $\Omega^{\mathrm{FT}}(\mathbf{q})$ is the Fourier transformation of $\Omega(\mathbf{r})$, and

$$G(\mathbf{q})=\left\langle \sum_m \sum_n e^{-i(\mathbf{q}\cdot\mathbf{R}_m-\mathbf{q}^*\cdot\mathbf{R}_n)}\right\rangle \quad (6)$$

is the geometrical factor depending on the dot positions. $\mathbf{q}=\mathbf{k}_f-\mathbf{k}_i$ is the complex scattering vector corrected to refraction and absorption in the undisturbed system.

It is well known from several structural studies of SiGe quantum dots in SiGe/Si superlattices[17–20] that the positions of the dots are well correlated vertically. Since in a GISAXS scan the angles of incidence and exit of the radiation with respect to the sample surface are kept constant, the coefficient $|t_i t_f|^2$ is constant, too, and the intensity of a GISAXS scan is proportional to the quantity

$$I(\mathbf{Q}_\parallel,Q_z)=|\Omega^{\mathrm{FT}}(\mathbf{Q}_\parallel,q_z)|^2 G_\parallel(\mathbf{Q}_\parallel), \quad (7)$$

where

$$\mathbf{Q}=\mathbf{K}_f-\mathbf{K}_i$$

is the scattering vector in vacuum and

$$G_\parallel(\mathbf{Q}_\parallel)=\left\langle \sum_{m=1}^{N}\sum_{n=1}^{N} e^{-i\mathbf{Q}_\parallel\cdot(\mathbf{X}_m-\mathbf{X}_n)}\right\rangle \quad (8)$$

is the lateral geometrical factor of the dot distributions, $\mathbf{X}_m$ is the random lateral position vector of the mth dot (the same for all the dots in a vertical stack) and N is the number of the dots at the irradiated part of a single interface. The horizontal components $\mathbf{Q}_\parallel$ and $\mathbf{q}_\parallel$ of the scattering vectors $\mathbf{Q}$ and $\mathbf{q}$ are equal, and the vertical components Q_z and q_z differ due to refraction.

Let us introduce the conditional probability $w(\mathbf{x})$ per unit area of finding a dot in lateral position $\mathbf{x}$ under the condition that the origin (0,0) is occupied by another dot. Then the lateral geometrical factor is

$$G_\parallel(\mathbf{Q}_\parallel)=N[1+w^{\mathrm{FT}}(\mathbf{Q}_\parallel)], \quad (9)$$

where w^{FT} is the Fourier transformation of w. For a large dot distance

$$\lim_{x\to\infty} w(\mathbf{x})=\frac{N}{S}\equiv n_0$$

holds (S is the irradiated sample surface area and n_0 is the two-dimensional density of the dots). If we denote

$$p(\mathbf{x})=w(\mathbf{x})-n_0$$

as the pair-correlation function of the dot positions, we obtain for the scattered intensity

$$I(\mathbf{Q}_\parallel, Q_z) = |\Omega^{\mathrm{FT}}(\mathbf{Q}_\parallel, q_z)|^2 S n_0 [1 + p^{\mathrm{FT}}(\mathbf{Q}_\parallel) + 4\pi^2 n_0 \delta(\mathbf{Q}_\parallel)]. \tag{10}$$

The last term of the right-hand side of this expression represents an infinitely narrow peak that contributes only to the coherently scattered intensity, and therefore it can be neglected in the expression for the intensity of diffuse scattering.

The aim of a GISAXS study is to determine both the shape of the dots and their distribution at the interfaces. As was shown previously,[15] the dot shape can be distinguished from the correlation of the dot positions performing an inverse two-dimensional Fourier transform of the GISAXS intensity profile

$$J(\mathbf{x}; Q_z) = \frac{1}{4\pi^2} \int d^2\mathbf{Q}_\parallel I(\mathbf{Q}_\parallel, Q_z) e^{i\mathbf{Q}_\parallel \cdot \mathbf{x}}. \tag{11}$$

Inserting from Eq. (10) we obtain after some algebra

$$J(\mathbf{x}; Q_z) = S n_0 [\Phi(\mathbf{x}; q_z) + p(\mathbf{x}) \otimes \Phi(\mathbf{x}; q_z)], \tag{12}$$

where

$$\Phi(\mathbf{x}; q_z) = \frac{1}{4\pi^2} \int d^2\mathbf{Q}_\parallel |\Omega^{\mathrm{FT}}(\mathbf{Q}_\parallel, q_z)|^2 e^{i\mathbf{Q}_\parallel \cdot \mathbf{x}} \tag{13}$$

and $\otimes$ means the convolution. Since the dots do not intersect, the pair-correlation function for small $|\mathbf{x}|$ equals $-n_0$ and thus the second term on the right-hand side of Eq. (12) yields a constant contribution to $J(\mathbf{x}; q_z)$ for small $|\mathbf{x}|$. Then, this contribution does not depend on $\mathbf{x}$ and it can be estimated to

$$|p(\mathbf{x}) \otimes \Phi(\mathbf{x}; q_z)| \lesssim \Theta V h_{\mathrm{eff}},$$

where Θ is the coverage of the interface by the dots, V is the dot volume and h_{eff} is an effective dot height depending on the shape of the dot. Therefore, for smaller $|\mathbf{x}|$, the shape of the function J depends only on the dot shape and not on the correlation of the dot positions.

For larger $|\mathbf{x}|$, the first term in Eq. (12) is zero. If we assume that the dot distance is much larger than the lateral dot size, the convolution in Eq. (12) can be replaced by a simple product

$$p(\mathbf{x}) \int d^2\mathbf{x}\, \Phi(\mathbf{x}; q_z) = \mathrm{const} \times p(\mathbf{x});$$

thus, for larger $|\mathbf{x}|$, the function $J(\mathbf{x})$ is proportional to the pair correlation function $p(\mathbf{x})$.

If the dots lie at the free sample surface, the above theoretical description of the scattering has to be changed. In this case, the matrix element

$$\langle E_f^{(A)} | \hat{\mathbf{V}}_{B,\mathrm{dots}} | E_i^{(A)} \rangle$$

contains the undisturbed wave fields above the sample surface,

$$|E_i^{(A)}\rangle = e^{i\mathbf{K}_i \cdot \mathbf{r}} + r_i e^{i\mathbf{K}_{iR} \cdot \mathbf{r}},$$

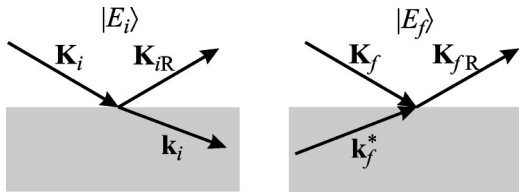

FIG. 1. Sketch of the undisturbed wave fields.

$$|E_f^{(A)}\rangle = e^{i\mathbf{K}_f \cdot \mathbf{r}} + r_f^* e^{i\mathbf{K}_{fR} \cdot \mathbf{r}},$$

where $\mathbf{K}_{iR}$ and $\mathbf{K}_{fR}$ are the wave vectors of the reflected waves belonging to $\mathbf{K}_i$ and $\mathbf{K}_f$, respectively, and $r_{i,f}$ are the Fresnel reflection coefficients corresponding to the waves $\mathbf{K}_{i,f}$. The undisturbed wave fields are sketched in Fig. 1. Repeating the procedure leading to Eqs. (10)–(13) we find that, in these formulas, the function $|\Omega^{\mathrm{FT}}(\mathbf{Q}_\parallel, q_z)|^2$ must be replaced by

$$\Psi(\mathbf{Q}_\parallel, Q_z) = |\Omega^{\mathrm{FT}}(\mathbf{Q}_\parallel, Q_z) + r_i r_f \Omega^{\mathrm{FT}}(\mathbf{Q}_\parallel, -Q_z) + r_i \Omega^{\mathrm{FT}}(\mathbf{Q}_\parallel, \tilde{Q}_z) + r_f \Omega^{\mathrm{FT}}(\mathbf{Q}_\parallel, -\tilde{Q}_z)|^2,$$

$$Q_z = K_{fz} - K_{iz}, \quad \tilde{Q}_z = K_{fz} + K_{iz}. \tag{14}$$

The four terms in the right-hand side of Eq. (14) describe four possible processes that take place at the surface. For instance, the third term gives the amplitude of the following process: reflection of the incident wave on the surface of the undisturbed system and subsequent scattering of the reflected wave by a dot.[14] The processes are presented by scattering vectors with different z components; the total scattering amplitude is a coherent sum of the contributions of individual processes.

III. EXPERIMENTAL RESULTS

A. Sample growth

The investigated Si/SiGe multilayer sample was grown by solid-source molecular beam epitaxy on a (001) Si substrate with a miscut of 2° along an azimuth 1.8° off the [001] direction. 20 periods consisting of a nominally 2.5 nm thick $Si_{1-x}Ge_x$ layer ($x_{\mathrm{Ge}} = 0.45$) and a 10 nm thick Si spacer layer were deposited at a substrate temperature of 550°C. On top of the last Si spacer layer five monolayers of pure Ge were deposited at 500°C.[21] Under these growth conditions, the miscut-induced surface steps form so-called step bunches,[22–25] i.e., ripples with a preferential size are formed at the growth surface, which are accompanied by strain fields influencing the nucleation of SiGe islands. It was intended to use these step bunches in order to obtain a more regular island arrangement and hence a narrower distribution of the island sizes.[26]

From high-resolution x-ray diffraction experiments it is evident that Ge-rich islands form within the multilayer. Cross-sectional transmission electron microscopy shows a rippled surface with a lateral period of about 120 nm and a height modulation of about 1.5 nm.

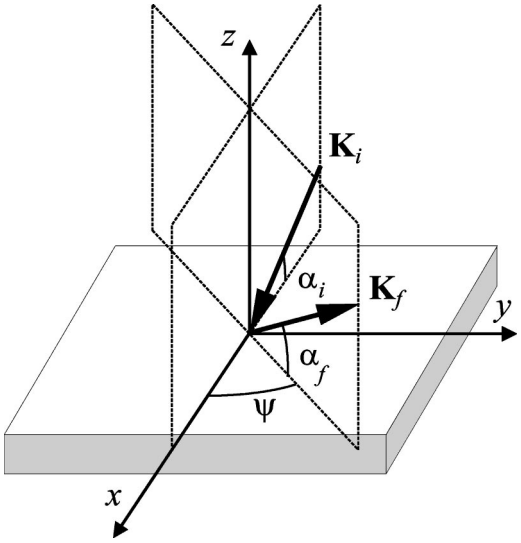

FIG. 2. Sketch of the GISAXS geometry.

B. GISAXS measurements

The GISAXS experiments were carried out at the TROÏKA II undulator beam line at the ESRF, Grenoble, using an x-ray wavelength of $\lambda = 0.15545$ nm. The diffusely scattered intensity from the islands was measured by a position-sensitive detector (PSD) oriented parallel to the sample surface. During a GISAXS scan the incidence and exit angles $\alpha_{i,f}$ of the primary and the scattered beam were kept constant and the scattered intensity has been measured as a function of the in-plane angle ψ (see Fig. 2). The angles $\alpha_{i,f}$ were chosen so that the scan trajectory in reciprocal space passed the coherent truncation rod in a very small distance $Q_x = 5.1 \times 10^{-3}$ nm^{-1}, in order to exclude the specular intensity peak from the measurements. Series of GISAXS scans were recorded for different $\alpha_{i,f}$ (i.e., for different Q_z's) and for azimuthal positions of the sample ranging from 0° to 180°, in steps of 5°. From the scans measured at a given Q_z we constructed a two-dimensional intensity distribution in the Q_x-Q_y plane. The resulting in-plane reciprocal-space maps are shown in Fig. 3. Performing the numerical two-dimensional Fourier transformations of these distributions after Eq. (11), we obtained the functions $J(\mathbf{x};Q_z)$ shown in Fig. 4.

For small $|\mathbf{x}|$ we have compared the values of J with a simple model assuming that the dots have the shape of an upper half of an ellipsoid. From the fit of function J to that model we determined the lateral half-axes of the ellipsoid a and b $(a>b)$, the vertical half-axis c (the dot height) and the azimuthal angle α of the longer axis of the ellipsoid with respect to the [110] direction. The quality of the fits can be judged from Figs. 5(a),(b), where we have plotted radial cuts from the two-dimensional distributions of J shown in Fig. 4 in the azimuthal directions $\phi = 45°$ and 135° with respect to [110] (indicated by the arrows in Fig. 4), along with their theoretical fits. The azimuthal direction of the miscut was $\phi_{\text{miscut}} \approx 133°$.

As follows from Table I, the values of a, b, and c depend on Q_z. This fact can be ascribed to the dependence of the x-ray information depth Λ on Q_z, which is defined as $\Lambda = 1/\text{Im}(q_z)$. The information depth ranges from 10 nm to about 1 μm (see Table I). For the smallest Q_z value, i.e., the smallest information depth Λ, only the topmost dot layer is probed by the x rays, and consequently the obtained parameters are those of the islands of the surface. With increasing Λ we obtain parameters of the dot shape that represent an

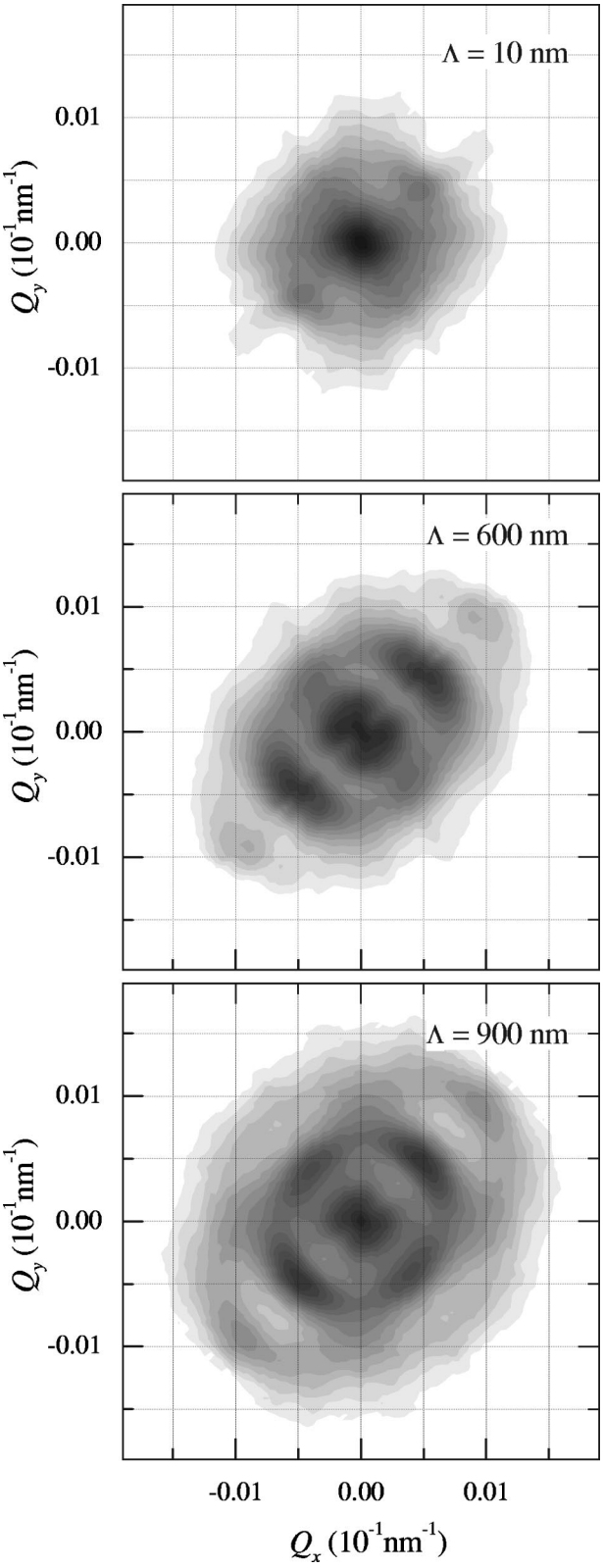

FIG. 3. In-plane intensity distributions measured in GISAXS geometry for three different information depths Λ.

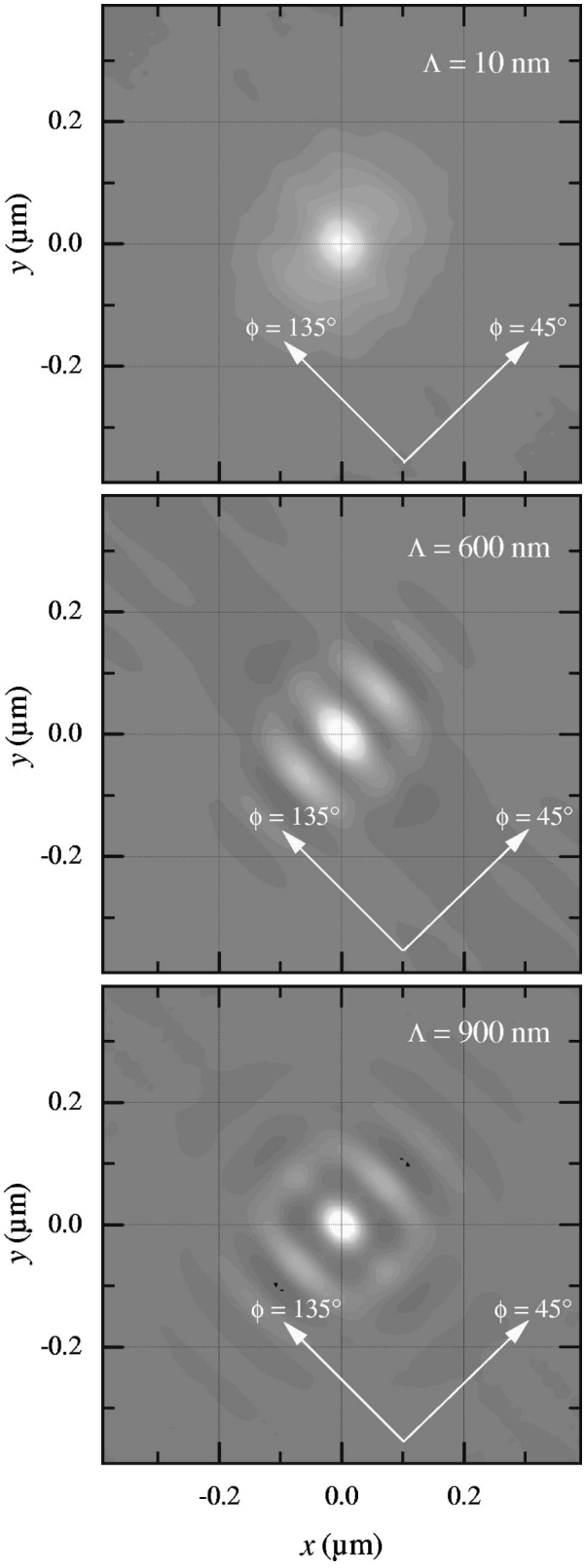

FIG. 4. The function $J(x,y;Q_z)$ obtained from the GISAXS data for three different information depths Λ.

average over all dot layers weighted by the actual x-ray intensities inside the sample.

The measurement with the smallest Λ was analyzed using Eq. (14), since, in this case, the information depth is smaller than the superlattice period. In this measurement, the values

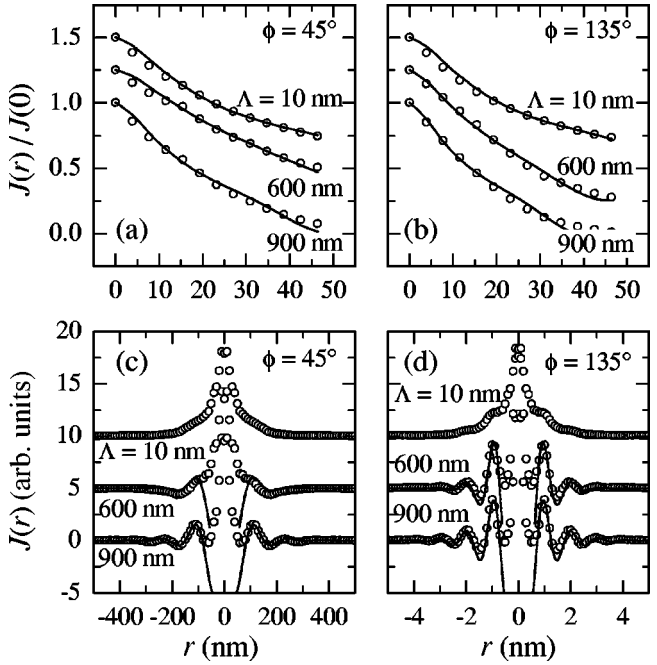

FIG. 5. (a,b) Measured (points) values of J in the region for small r for two different azimuthal directions ϕ and three different information depths Λ and their fits using the model of ellipsoidal dots (thin lines). (c,d) For large r the experimental data for J (circles) have been fitted using the short-range-order model of the dot arrangement (lines).

of a and b were found to be similar, so that the azimuthal angle α of the axis a could not be determined with sufficient accuracy.

The pair-correlation function of the dot positions was obtained from the radial cuts of J for larger $|\mathbf{x}|$. We have compared these cuts with the one-dimensional pair-correlation function assuming a short-range-order model of the dot distribution[27]

$$p^{\mathrm{FT}}(Q)=2\,\mathrm{Re}\left(\frac{\xi(Q)}{1-\xi(Q)}\right), \tag{15}$$

where $\xi(Q)$ is the characteristic function of the random distribution of the distances L of neighboring dots:

$$\xi(Q)=\langle e^{-iQL}\rangle.$$

In the simulation we have assumed a Γ distribution of the dot distances. From the fits of the experimental cuts to the theory shown in Figs. 5(c),(d), we have determined the mean dot distance $\langle L\rangle$ and the order m of the Γ distribution as func-

TABLE I. The parameters of the dot shapes following from the GISAXS and AFM measurements.

Re(q_z) (nm^{-1})	Λ (nm)	a (nm)	b (nm)	c (nm)	α (deg)
AFM 1		35±2	28±2	4.0±2.0	40±10
AFM 2		31±4	29±5	5.4±2.0	40±10
0.64	10	38±6	36±6	4.5±0.4	
0.92	600	35±2	23±2	2.6±0.1	51±6
1.15	900	25±2	20±2	2.3±0.2	48±20

TABLE II. Mean distances $\langle L \rangle$ of the dots and the order m of their Γ distribution determined from the GISAXS and AFM data in various azimuthal directions.

Λ (nm)	ϕ (deg)	$\langle L \rangle$ (nm)	m
AFM 1	45	102 ± 2	22
AFM 1	135	108 ± 5	48
AFM 2	45	115 ± 10	10
AFM 2	135	100 ± 10	13
GISAXS $\Lambda = 10$ nm			
600 nm	45	120 ± 5	5
600 nm	135	101 ± 5	10
900 nm	45	120 ± 5	9
900 nm	135	101 ± 5	14

tions of the azimuthal angle ϕ. The results are listed in Table II. The function J obtained from the GISAXS scans with the smallest Λ exhibits no lateral maxima, so that the determination of $\langle L \rangle$ and m was not possible. Likely, the number of the irradiated interfaces, and consequently, the number islands, is too small in this case, so that the wave scattered from the dots is weak and may be blurred by, e.g., scattering from surface roughness with larger lateral correlation length. From the table, the tendency of decrease of m towards the free surface is obvious. However, this is probably an artifact due to the increase of the influence of the surface roughness scattering with decreasing Λ that smears out the modulation of J.

From the data shown in Table II it follows that the dots are arranged approximately in a square array along $\langle 100 \rangle$ directions; however, the dispersion of the dot distances in the [100] direction parallel to the miscut is smaller than that perpendicular to the miscut direction due to the step bunching during growth of the multilayer.[21,26] The positions of the dots obey the short-range-order model very well.

C. Comparison with AFM

AFM pictures taken at different position of the sample surface are shown in Fig. 6. In the upper panel, regions with rather round dots with a good lateral correlation (upper left rectangle) exist, besides regions where the dots are rather randomly distributed (right rectangle). Furthermore, regions where the dots are aligned in ''chains'' along the step bunches are visible, but those chains are not always straight but do end or are bent (lower left rectangle). The lower two panels in Fig. 6 show two AFM images on a smaller scale that have been used for the statistical evaluation of the island's shape and arrangement. ''AFM 1'' shows round islands, and those in ''AFM 2'' are clearly elongated. Also the dot positions appear less regular in the second panel as compared to the first one. The reason for this anisotropy lies in the fact that the island positions and sizes are influenced by the step-bunching pattern, which is not completely regular. The lateral ordering of islands on step-bunched samples is, however, superior to those grown on nonvicinal substrates.

The AFM data can be analyzed in a way very similar to the analysis of the GISAXS data shown in the previous paragraph. If the scanned sample surface is large enough, the

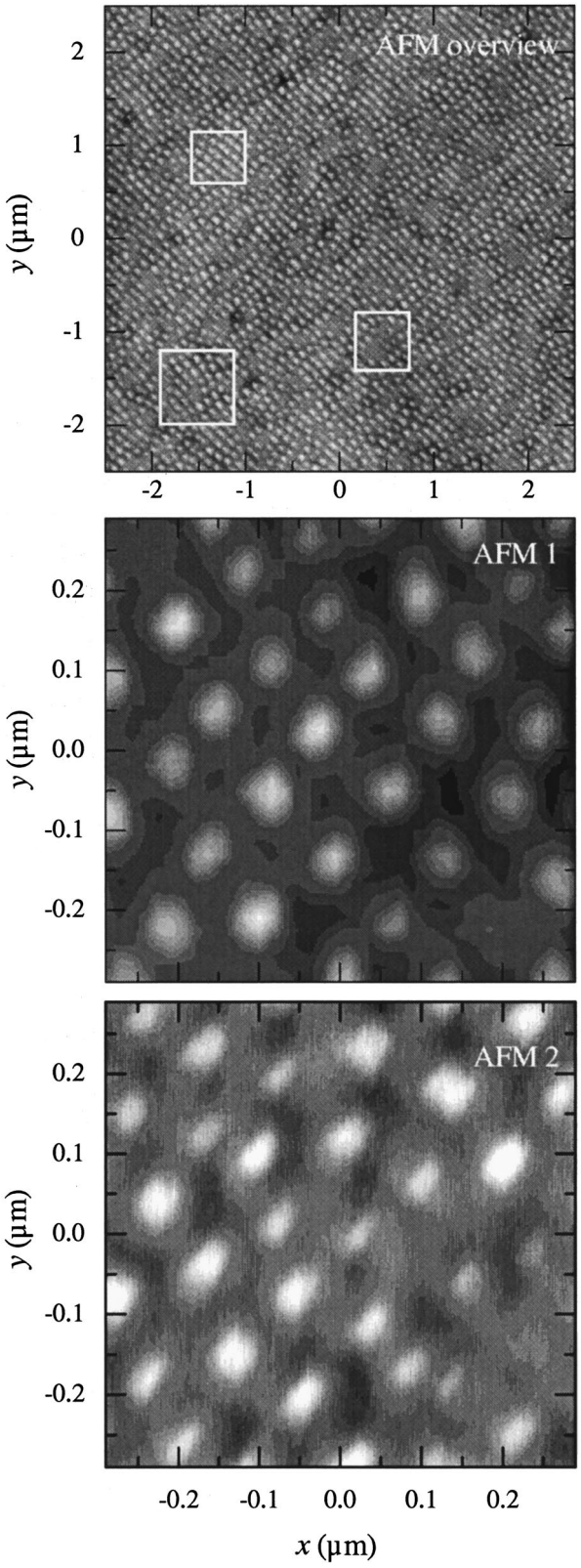

FIG. 6. AFM images of the sample surface, recorded at different spots. The upper panel shows an overview, with different regions with regular island arrangement (upper left rectangle) and almost random island arrangement (right rectangle), and regions where the dots are aligned in chains along step bunches, which are, however, not straight throughout the image (lower left rectangle). The lower two panels show two AFM images on a smaller scale that have been used for a statistical analysis of the island shape and arrangement.

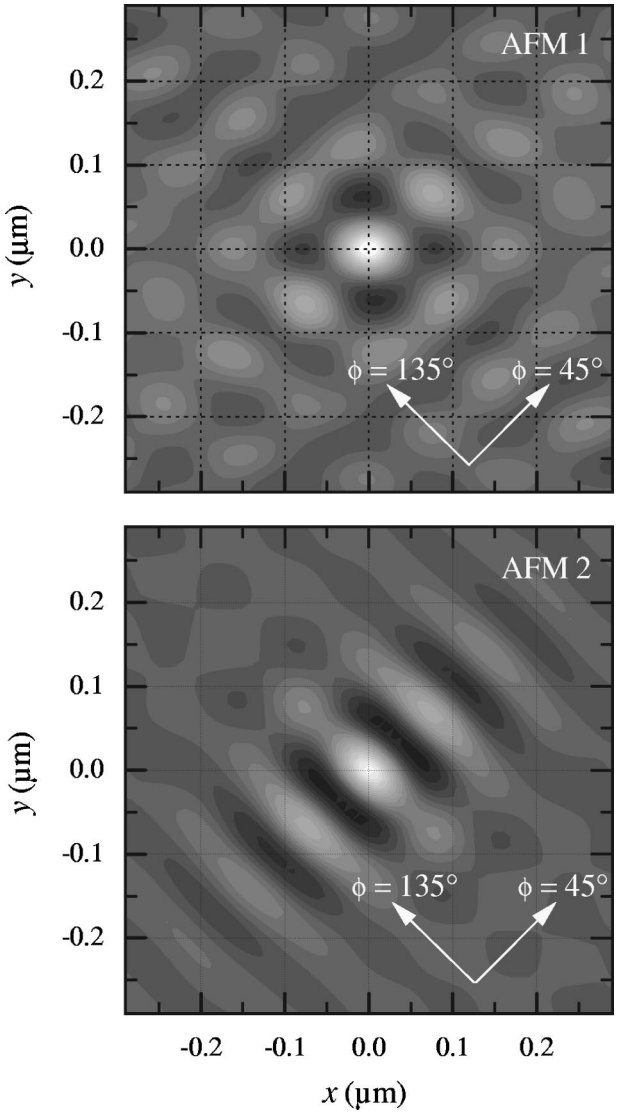

FIG. 7. Autocorrelation function $J(\mathbf{x};0)$ obtained from the measured AFM data.

Fourier transformation of the AFM signal $z(\mathbf{x})$ can be expressed as an ''intensity'' distribution in reciprocal space similarly to Eq. (7):

$$I(\mathbf{Q}_\parallel,0)=\int d^2\mathbf{x}\, z(\mathbf{x})e^{-i\mathbf{Q}_\parallel\cdot\mathbf{x}}=|\Omega^{\mathrm{FT}}(\mathbf{Q}_\parallel,0)|^2 G_\parallel(\mathbf{Q}_\parallel). \tag{16}$$

Performing the inverse Fourier transformation of $I(\mathbf{Q}_\parallel,0)$ we obtain the autocorrelation function of the surface

$$J(\mathbf{x};0)=\frac{1}{4\pi^2}\int d^2\mathbf{Q}_\parallel I(\mathbf{Q}_\parallel,0)e^{i\mathbf{Q}_\parallel\cdot\mathbf{x}}$$
$$=Sn_0[\Phi(\mathbf{x};0)+w(\mathbf{x})\otimes\Phi(\mathbf{x};0)] \tag{17}$$

shown in Fig. 7. This function is equivalent to the function J defined in Eq. (11) for GISAXS and $q_z=0$. In contrast to x-ray scattering data, we did not delete the δ-like peak in $I(\mathbf{Q}_\parallel,0)$ in the calculation of the Fourier transformation J and thus we obtained the expression for J containing the conditional probability $w(\mathbf{x})$ instead of the pair-correlation function $p(\mathbf{x})$. Repeating the same considerations as in the previous paragraph we find that

$$J(\mathbf{x};0)\approx Sn_0\Phi(\mathbf{x};0)$$

for small $|\mathbf{x}|$ and

$$J(\mathbf{x};0)\approx \mathrm{const}\times w(\mathbf{x})$$

for larger $|\mathbf{x}|$.

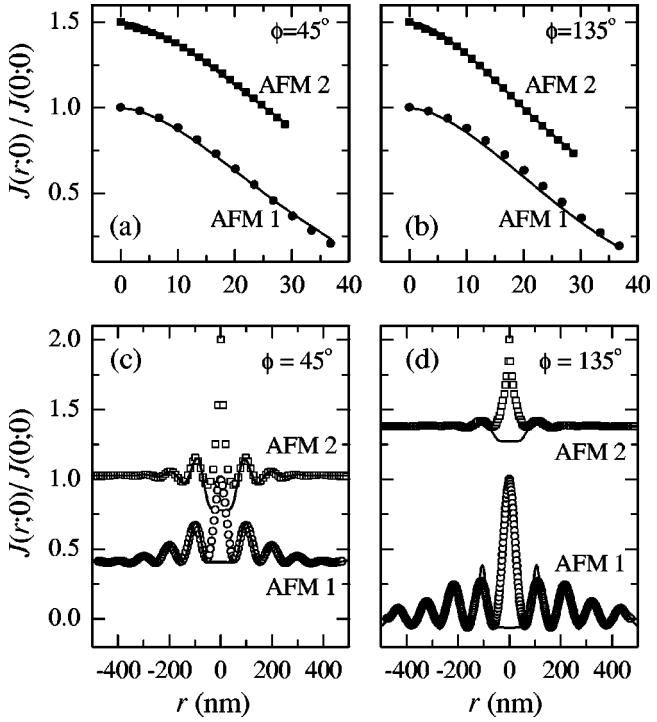

FIG. 8. (a,b) In the region of small r, cuts through the autocorrelation function $J(r;0)$ (points) for two different azimuths ϕ have been fitted using an ellipsoidal dot model. (c,d) For large r, $J(r;0)$ was fitted assuming a short-range-order distribution of the dot positions.

We have fitted radial cuts in different azimuths (indicated by the arrows in Fig. 7) through the autocorrelation function for small $|\mathbf{x}|$ using the same ellipsoidal dot shape model as for the analysis of the GISAXS data. The fits are plotted in Figs. 8(a),(b); the obtained parameters are given in Table I. The vertical half-axis c of the ellipsoidal dot shape can be determined from the autocorrelation function J of the AFM data only with larger error. In contrast to GISAXS, the shape of J normalized to the maximum value $J(0;0)$ does not depend on c at all and we have determined its value from the difference $J(0;0)-J(\infty;0)$. Within the ellipsoidal shape model the following relation holds:

$$\lim_{x\to\infty}[J(0;0)-J(\mathbf{x};0)]\approx\frac{1}{2}Sc^2\Theta.$$

An exact determination of the mean coverage Θ from the AFM picture is complicated by the fact that the bottom level of the surface between the dots is not well defined. If we determine Θ using the level $z=z_{\max}/2$, we obtain $\Theta\approx 0.1$, which yields $c=4.0$ nm.

For larger $|\mathbf{x}|$ we have compared the cuts of the autocorrelation function with the pair-correlation function following

from the short-range-order model (15) [see Figs. 8(c),(d)] and we determined the mean dot distances $\langle L \rangle$ as well as the order m of the Γ distribution of L (Table II) and the values are comparable to the GISAXS results.

The obtained parameters reflect in a more quantitative way the lateral inhomogeneity of the sample. There is a reasonable correspondence of the shape parameters with those obtained from the GISAXS data for the smallest information depth, but the results do not perfectly coincide. This demonstrates the different statistical probes of AFM and GISAXS. While the latter method gives better average values, the *shape* resolution of AFM is better in the size range of the SiGe islands of the investigated sample.

IV. CONCLUSIONS

In conclusion, we have demonstrated that GISAXS experiments on *buried and free-standing* islands can be quantitatively interpreted using a theoretical model based on the distorted-wave Born approximation. The experiments require the use of synchrotron radiation at undulator beam lines, and for their quantitative interpretation the recording of two-dimensional reciprocal-space maps in GISAXS geometry is needed. From these maps, autocorrelation spectra can be calculated, which were simulated using a short-range-order model of the dot positions and different models of the shape of the quantum dots. From the fits to the experimental data, finally the shape as well as the lateral correlation of the buried islands is obtained. Since the illuminated area is of the order of several mm^2, the GISAXS results represent a statistical average over a large number of dots. Additionally, GISAXS scans for sufficiently small information depth give information solely on the top layer of unburied Ge islands.

The same approach can be used to analyze AFM images in a statistical way. AFM and GISAXS are in some sense complementary methods for samples with self-organized islands and step bunches, which usually exhibit lateral inhomogeneities. While AFM gives a direct image of the islands and has a good resolution for determining the island shape, it is difficult to obtain parameters with sufficient statistics to represent the whole sample. For this task the nonlocal GISAXS method is ideally suited. On the other hand, the type of lateral inhomogeneity cannot be easily extracted from GISAXS data, but it is obvious from AFM images. The shape and correlation of *buried* dot layers are inaccessible by AFM, but it seems reasonable to assume that the general type of fluctuations is similar to those on the sample surface.

ACKNOWLEDGMENTS

This work was supported by the FWF, the BMWV, and the GMe, Vienna, and by the Grant Agency of the Czech Republic (No. 202/00/0354). The experiments were carried out at the TROÏKA II beamline of the ESRF, Grenoble, France. We thank D. Smilgies for his most valuable help with the beam-line setup and I. Kegel and T.H. Metzger for assistance with the experiment.

*Permanent address: Department of Solid State Physics, Faculty of Science, Masaryk University, 611 37 Brno, Czech Republic.

[1] D. Bimberg, M. Grundmann, and N. N. Ledentsov, *Quantum Dot Heterostructures* (Wiley, Chichester, 1999).
[2] For a series of articles on self-organized dots see Mater. Res. Bull. **23** (2) (1998).
[3] P. Sutter and M.G. Lagally, Phys. Rev. Lett. **81**, 3471 (1998).
[4] E. Mateeva, P. Sutter, and M.G. Lagally, Appl. Phys. Lett. **74**, 567 (1999).
[5] A.J. Steinfort, P.M.L.O. Scholte, A. Ettema, F. Tuinstra, M. Nielsen, E. Landmark, D.M. Smilgies, R. Feidenhans'l, G. Falkenberg, L. Seehofer, and R.L. Johnson, Phys. Rev. Lett. **77**, 2009 (1996).
[6] A.A. Darhuber, P. Schittenhelm, V. Holý, J. Stangl, G. Bauer, and G. Abstreiter, Phys. Rev. B **55**, 15 652 (1997).
[7] T.H. Metzger, I. Kegel, R. Paniago, and J. Peisl, J. Phys. D **32**, A202 (1999).
[8] Q. Shen and S. Kycia, Phys. Rev. B **55**, 15 791 (1997).
[9] I. Kegel, T.H. Metzger, P. Fratzl, J. Peisl, A. Lorke, J.M. Garcia, and P.M. Petroff, Europhys. Lett. **45**, 222 (1999).
[10] Th. Wiebach, M. Schmidbauer, M. Hanke, H. Raidt, R. Köhler, and H. Wawra, Phys. Rev. B **61**, 5571 (2000).
[11] M. Schmidbauer, Th. Wiebach, H. Raidt, M. Hanke, R. Köhler, and H. Wawra, Phys. Rev. B **58**, 10 523 (1998).
[12] J.R. Levine, J.B. Cohen, Y.W. Chung, and P. Georgopulos, J. Appl. Crystallogr. **22**, 528 (1989).
[13] J.R. Levine, J.B. Cohen, and Y.W. Chung, Surf. Sci. **248**, 215 (1991).
[14] M. Rauscher, R. Paniago, H. Metzger, Z. Kovats, J. Domke, J. Peisl, H.D. Pfannes, J. Schulze, and I. Eisele, J. Appl. Phys. **86**, 6763 (1999).
[15] J. Stangl, V. Holý, P. Mikulik, G. Bauer, I. Kegel, T.H. Metzger, O.G. Schmidt, C. Lange, and K. Eberl, Appl. Phys. Lett. **74**, 3785 (1999).
[16] S.K. Sinha, E.B. Sirota, S. Garoff, and H.B. Stanley, Phys. Rev. B **38**, 2297 (1988).
[17] J. Tersoff, C. Teichert, and M.G. Lagally, Phys. Rev. Lett. **76**, 1675 (1996).
[18] I. Daruka, A.-L. Barabasi, S.J. Zhou, T.C. Germann, P.S. Lomdahl, and A.R. Bishop, Phys. Rev. B **60**, R2150 (1999).
[19] F. Liu, S.E. Davenport, H.M. Evans, and M.G. Lagally, Phys. Rev. Lett. **82**, 2528 (1999).
[20] V. Holý, G. Springholz, M. Pinczolits, and G. Bauer, Phys. Rev. Lett. **83**, 356 (1999).
[21] J.H. Zhu, K. Brunner, and G. Abstreiter, Appl. Phys. Lett. **72**, 424 (1998).
[22] J. Tersoff, Y.H. Phang, Z. Zhang, and M.G. Lagally, Phys. Rev. Lett. **75**, 2730 (1995).
[23] C. Teichert, Y.H. Phang, L.J. Peticolas, J.C. Bean, and M.G. Lagally, in *Surface Diffusion: Atomistic and Collective Processes*, Vol. 360 of the NATO Advanced Study Institute Series B, edited by M. Tringides (Plenum, New York, 1997), p. 297.
[24] F. Liu, J. Tersoff, and M.G. Lagally, Phys. Rev. Lett. **80**, 1268 (1998).
[25] J.H. Zhu, K. Brunner, G. Astreiter, O. Kienzle, F. Ernst, and M. Rühle, Phys. Rev. B **60**, 10 935 (1999).
[26] J. Stangl, T. Roch, V. Holý, M. Pinczolits, G. Springholz, G. Bauer, I. Kegel, T.H. Metzger, J. Zhu, K. Brunner, G. Abstreiter, and D. Smilgies, J. Vac. Sci. Technol. (to be published).
[27] P.R. Pukite, C.S. Lent, and P.I. Cohen, Surf. Sci. **161**, 39 (1985).